CAAI Transactions on Intelligence Technology

WILEY

ORIGINAL RESEARCH OPEN ACCESS

Auto-ISC: Inter-Sample Contrastive Learning for Automated Curve Angle Calculation From Ultrasound

Chen Zhang[1] | Anh Hoang Phuc Nguyen[1] | Yongping Zheng[2] | Sai Ho Ling[1]

[1]School of Electrical and Data Engineering, University of Technology Sydney, Ultimo, New South Wales, Australia | [2]Department of Biomedical Engineering, The Hong Kong Polytechnic University, Hong Kong, China

Correspondence: Sai Ho Ling (Steve.Ling@uts.edu.au)

Received: 21 January 2026 | **Revised:** 15 April 2026 | **Accepted:** 13 May 2026

ABSTRACT

Scoliosis assessment has been increasingly supported by AI-assisted tools, enabling more efficient and standardised clinical workflows. However, existing ultrasound-based pipelines often suffer from limited generalisation and unstable performance. These limitations primarily arise from two challenges: (1) suboptimal segmentation under low-contrast and noisy imaging conditions, and (2) unreliable anatomical landmark identification due to missing or ambiguous features. To address these issues, we propose Auto-ISC, a novel two-stage automated ultrasound scoliosis assessment system. The first stage employs the ISC-Swin segmentation model, enhanced by an Inter-Sample Contrastive Bank (ISCB) to improve cross-sample feature consistency and class-level discrimination. The second stage introduces a dynamic pairing logic algorithm for accurate matching of thoracic vertebrae, enabling reliable downstream angle estimation. Experimental results demonstrate strong segmentation performance (Dice: 86.10%, IoU: 76.08%) and high agreement with manual measurements. The proposed method achieves low average absolute differences (ABS) (thoracic: 2.83° ± 2.16°; lumbar: 2.89° ± 2.55°) and strong correlations ($R^2 = 0.91$ for thoracic and 0.81 for lumbar). Overall, Auto-ISC provides a reliable and radiation-free solution for automated scoliosis assessment, with improved clinical applicability.

1 | Introduction

Scoliosis, a spinal deformity characterised by an "S" or "C"-shaped curvature exceeding 10°, poses a significant global health challenge [1–3]. Although Cobb angle measurement via X-ray remains the clinical gold standard [4], the associated ionising radiation raises safety concerns, particularly for repeated screenings [5]. In this field, AI has increasingly been applied to automate scoliosis diagnosis, predominantly using X-ray and MRI modalities [6–8]. In contrast, ultrasound imaging offers a safer and non-invasive alternative. Curve estimation methods based on spinous and transverse processes have shown good reliability [3, 9], though they often underestimate curve magnitude relative to X-ray measurements. Despite its promise, ultrasound imaging faces intrinsic limitations, such as low contrast, high noise, and anatomical variability, that make automated Ultrasound Curve Angle (UCA) estimation particularly challenging [10]. Consequently, accurate segmentation is critical for overcoming these barriers and enabling reliable UCA assessment.

Recent advances in scoliosis assessment have explored object detection and landmark-based methods on radiographs [7, 11, 12]. Meanwhile, the emergence of the Scolioscan system has accelerated the development of ultrasound-based solutions. RankNet was proposed to select high-quality depth images from ultrasound scans [13], leading to segmentation-based approaches [14–16] and quality enhancement techniques [17]. However, many studies rely on limited datasets and often fail to generalise across different scoliosis severities. Furthermore, a common

This is an open access article under the terms of the Creative Commons Attribution License, which permits use, distribution and reproduction in any medium, provided the original work is properly cited.

© 2026 The Author(s). *CAAI Transactions on Intelligence Technology* published by John Wiley & Sons Ltd on behalf of The Institution of Engineering and Technology and Chongqing University of Technology.

limitation in existing methods is the incorrect pairing of thoracic vertebrae—a fixed number of 12 thoracic vertebral pairs is expected per patient [2, 18, 19]—which results in inaccurate angle calculations due to segmentation or matching errors.

To address these challenges, our previous work introduced ISC-Swin [20], a Swin Transformer-based framework for ultrasound spine feature segmentation, which integrates an inter-sample contrastive learning strategy to enhance pixel-level feature discrimination. The proposed Inter-Sample Contrastive Bank (ISCB) enables effective modelling of cross-sample feature relationships, significantly improving robustness to low contrast, speckle noise, and anatomical variability in ultrasound images. Notably, this prior work focuses solely on the segmentation task and has been rigorously validated for accurate spine feature extraction [20]. Building upon this foundation (As Figure 1 shows), we propose Auto-ISC, a two-stage fully automated ultrasound-based scoliosis assessment system. In the first stage, anatomical structures are localised and standardized, while in the second stage, the extracted spine features are further translated into clinically relevant scoliosis measurements, such as the UCA, enabling accurate and reliable curvature estimation. As a result, our approach achieves state-of-the-art performance, with ISC-Swin reaching a Dice score of 86.10% and IoU of 76.08%, outperforming Transformer-based and U-Net baselines (Table 1). In addition, the Auto-ISC demonstrated excellent concordance with manual measurements, evidenced by low average absolute difference (thoracic: 2.83° ± 2.16°; lumbar: 2.89° ± 2.55°), under the same experimental settings used for comparison with existing methods. These results affirm the clinical reliability of the method and its promise as a viable, radiation-free alternative for scoliosis assessment.

Our main contributions are as follows:

1. We present Auto-ISC, an automated two-stage ultrasound scoliosis assessment system that integrates segmentation and pairing algorithms to achieve reliable UCA measurements and streamline clinical reporting.
2. We introduce a dynamic pairing logic algorithm that correctly matches thoracic vertebrae pairs, resolving the common issue of incorrect thoracic level identification that

TABLE 1 | Comparison of model performance on bone feature detection (%).

Model	DSC	IoU
SATR [21]	85.81	75.81
SegFormer [22]	83.67	72.66
Swin-Unet [23]	84.50	73.20
H2Former [24]	84.70	73.70
TransUnet [25]	84.00	72.90
TransDeepLab [26]	83.50	71.60
U-Net [27]	81.90	69.20
U-Net++ [28]	82.20	69.40
SSAT [15]	85.60	74.50
ISC-Swin	**86.10**	**76.08**

Note: The best result for each metric is highlighted.

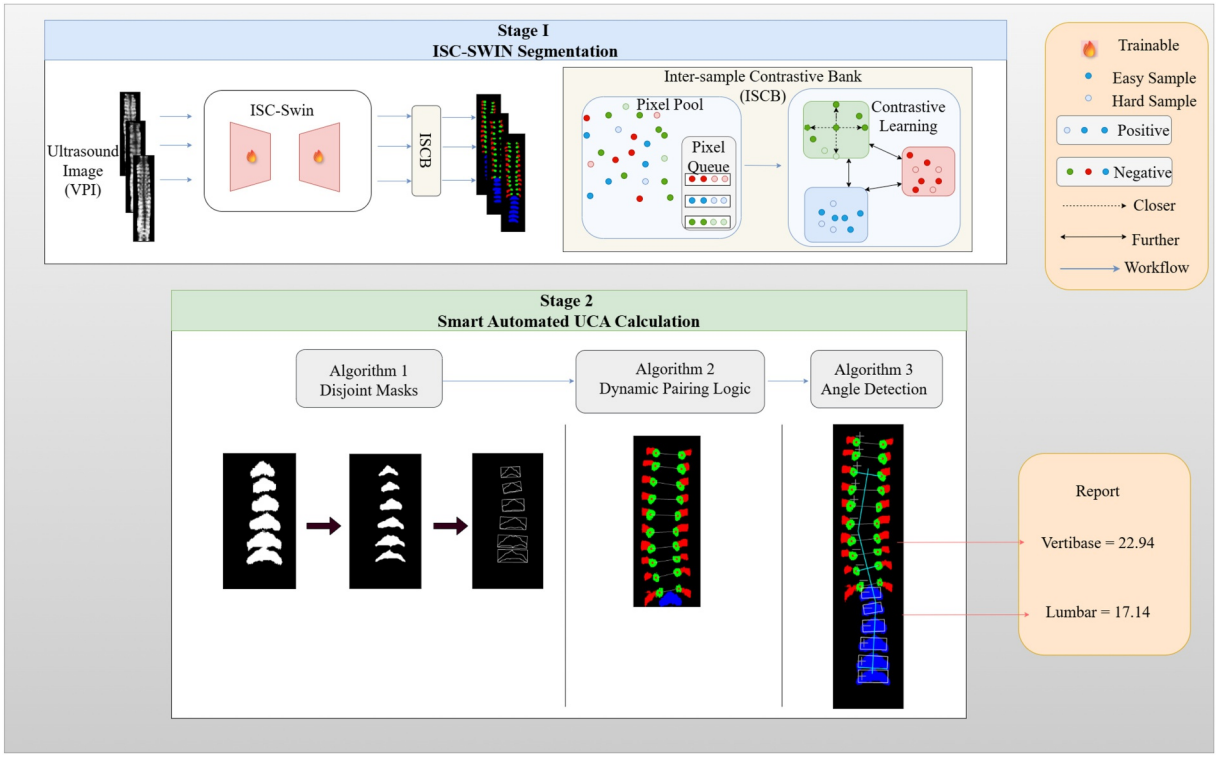


FIGURE 1 | Overview of the proposed Auto-ISC framework. The system consists of two stages: (1) ISC-Swin segmentation with an Inter-Sample Contrastive Bank (ISCB) for class-enhanced feature learning; (2) smart automated UCA calculation for robust vertebral matching and UCA estimation, which has three algorithms.

has plagued previous approaches and directly affected angle calculation accuracy.

3. Our experiments show strong segmentation results (Dice: 86.10%, IoU: 76.08%) and high agreement with manual UCA measurements (thoracic: 2.83° ± 2.16°, lumbar: 2.89° ± 2.55°; R^2: 0.91/0.81).

2 | Related Works

2.1 | Challenges in Ultrasound Image

Several studies have highlighted technical challenges specific to ultrasound-based spinal assessment. Anatomical obstructions (e.g., scapula), high body mass index (BMI), and abnormal spinal curvature can substantially degrade image quality, particularly in the lumbar region [3, 29, 30]. Adipose tissue attenuates ultrasound signals at approximately 0.63 dB/cm, reducing visibility of deeper structures and complicating the detection of key anatomical landmarks [31–33]. Consequently, ultrasound-guided spine assessments often exclude patients with a BMI above 25–30 kg/m^2 due to insufficient signal penetration [34]. Currently, research has found that accurate segmentation of vertebral landmarks—particularly transverse processes (TPs)—is essential for reliable UCA calculations [35].

2.2 | Development of Automated Assessment

Traditional convolutional neural networks (CNNs), such as U-Net, have been widely adopted for medical image segmentation due to their strong local feature learning capabilities [36–38]. More recently, transformer-based architectures, including SSAT-Swin [15] and Structure-Affinity Transformers [21, 39], have demonstrated promising performance by capturing long-range dependencies through attention mechanisms. In parallel, image enhancement and denoising techniques have been explored to improve feature visibility in ultrasound images [17, 40], while other studies focus on addressing feature incompleteness caused by the limited field-of-view (FOV) [41]. Despite these advances, a key limitation remains: suboptimal segmentation often leads to incomplete landmark detection, particularly when thoracic points (TPs) are partially occluded or absent, resulting in unreliable UCA measurements [42, 43]. Consequently, developing more robust segmentation methods and more precise landmark detection strategies, together with intelligent post-processing for accurate angle estimation, remains an important and open research challenge [44].

3 | Methods and Materials

3.1 | Segmentation Structure

Following our previous work [20], the ISC-Swin architecture builds on the strong multi-scale feature extraction of the Swin Transformer and introduces an Inter-Sample Contrastive Bank (ISCB) to explicitly model inter-sample relationships for improved pixel-level discrimination (as Figure 2 shows). During training, the Swin Transformer produces hierarchical feature maps from ultrasound images of scoliosis. A sampling scheme then selects both “hard” and “easy” pixel examples, which are stored in a class-aware Pixel Pool and merged into a persistent Pixel Queue that collects representative features from all batches (as Figure 3 shows). The ISCB calculates a modified contrastive

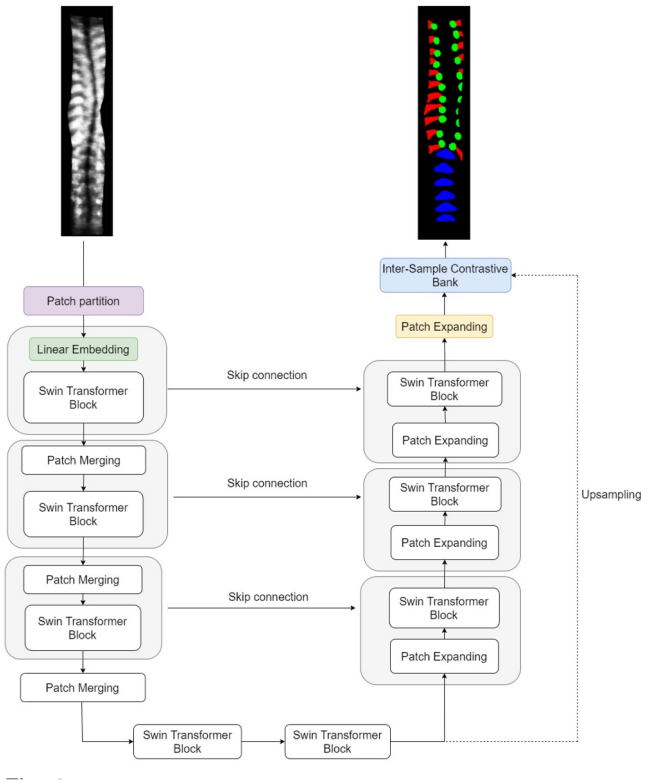


FIGURE 2 | The pipeline follows an encoder–decoder architecture. An inter-sample contrastive bank is integrated at the high-level feature stage to enhance pixel-wise representation by leveraging cross-sample contrastive learning, improving robustness to noise and anatomical ambiguity.

loss by comparing positive and negative samples from this cross-batch memory. This encourages the network not only to group pixels of the same class within a single image but also to clearly separate pixels across different images. This cross-sample contrastive mechanism is particularly beneficial for low-contrast and noisy ultrasound data, as it allows the model to learn global class patterns and subtle differences between images that are often overlooked by conventional within-image losses.

3.1.1 | *Pixel Pool*

Following the sampling phase, pixels taken from the current batch's multi-scales are arranged by class in the Pixel Pool.

3.1.2 | *Pixel Queue*

The Pixel Queue in the Pixel Pool maintains representative features from the same class across images. The queue is updated throughout the training phase to guarantee that it contains the most representative characteristics for every class.

3.2 | Pixel Contrast Loss

Contrastive learning typically employs the InfoNCE loss [45], defined as:

$$\mathcal{L}I^{\mathrm{NCE}} = -\log \frac{\exp\left(v^{\top} t/\tau\right)}{\exp\left(v^{\top} t/\tau\right) + \sum v_n \in \mathcal{N} \exp\left(v_n t/\tau\right)}, \quad (1)$$

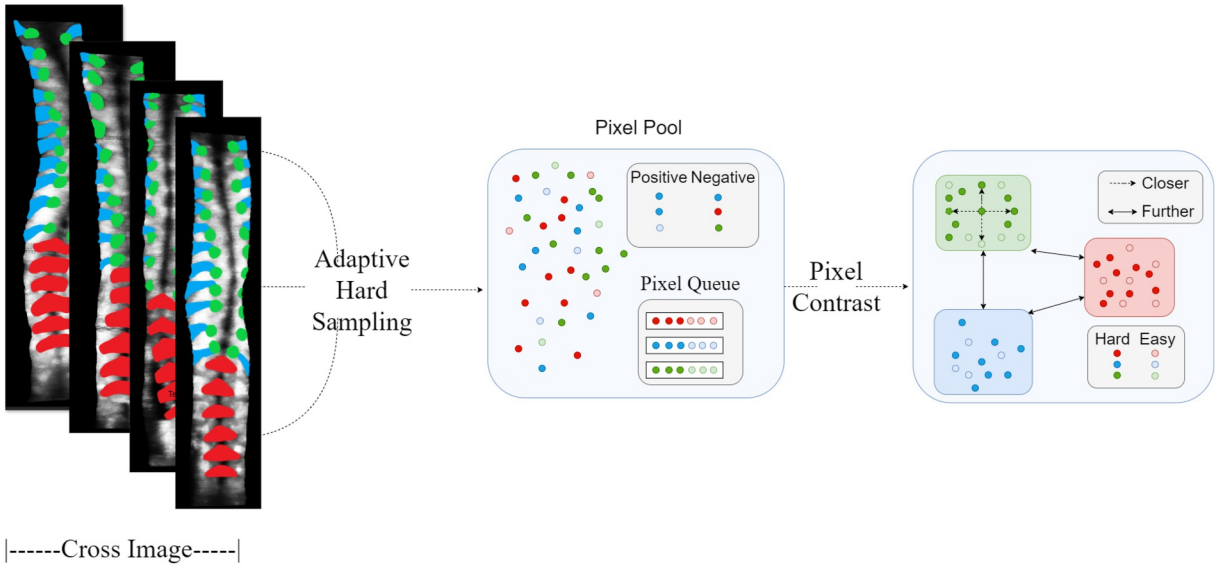


FIGURE 3 | The structure of the ISCB. An adaptive sampling strategy is first employed to select representative pixels from feature maps, which are then stored in a pixel pool. A pixel queue further maintains these samples across different batches to enable inter-sample interaction. Subsequently, a pixel-wise contrastive learning scheme is applied to enforce discriminative feature learning across classes, enhancing inter-class separability and improving the robustness of pixel-level representations.

where v and t are the ell_2-normalised embeddings of an anchor, and its positive sample, respectively, and $\mathcal{N}$ denotes the set of negative samples. The temperature τ controls the sharpness of the similarity distribution and is set to 0.1 following standard practice in supervised contrastive learning. This loss encourages higher similarity between positive pairs while reducing similarity with negatives.

For segmentation, the contrastive objective is extended to pixel-level representations, where pixels from the same class form positive pairs, and others act as negatives. The pixel-wise contrastive loss is given by:

$$\mathcal{L}i^{\mathrm{NCE}} = -\frac{1}{|P_i|}\sum t_j \in P_i \log\frac{\exp\left(i^{\top}t_j/\tau\right)}{\exp\left(i^{\top}t_j/\tau\right)+\sum_{t_k\in N_i}\exp\left(i^{\top}t_k/\tau\right)}. \quad (2)$$

This formulation maximises the similarity between each anchor pixel i and its positive samples t_j, while minimising similarity with negative samples t_k, promoting discriminative pixel-level feature representations.

Compared to conventional contrastive learning that operates within a single image, the proposed ISCB introduces cross-sample interaction through a class-aware memory queue. This enables the model to capture global class distributions across different patients, which is particularly beneficial for ultrasound images with high noise and low contrast.

3.3 | Dynamic Pairing Logic Algorithm

The overall Dynamic Pairing Logic algorithm includes a Disjoint Masks Algorithm with a Dynamic Pairing Logic (DPL) algorithm.

To address the challenge of conjoint landmarks in TBFs and LBFs [42], as Algorithm 1 shows the Disjoint Masks Algorithm (DMA) operates by computing the shortest distance from each pixel in a mask to the background, creating a distance map Figure 4b. Applying a threshold to this map trims the mask margins, effectively separating connected landmarks. For TBFs, the resulting mask centroids are used for the Dynamic Pairing Logic, while the outer bounding boxes are adapted for LBFs (Figure 4).

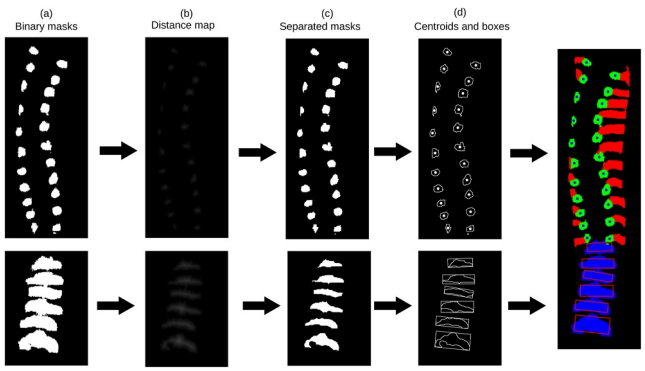


FIGURE 4 | Schematic of the Dynamic Pairing Logic (DPL) algorithm. Given two vertically sorted centroid sets from the left and right spinal features, the algorithm performs sequential matching based on vertical proximity.

ALGORITHM 1 | Disjoint Masks algorithm

Require: Binary mask image M, threshold scaling factor α
Ensure: List of separated mask contours C
1: Compute distance map of masks by Euclidean distance.
2: Threshold the distance map using α to get smaller masks.
3: Compute contours.
4: Return list of contours.

In addition, as Algorithm 2 shows the Dynamic Pairing Logic (DPL) algorithm operates on two ordered sets of centroids, including $L = l_1, ..., l_n$ for the left side and $R = r_1, ..., r_m$ for the

right side, each sorted by their vertical coordinates (y) along the spine. Two indices (li, ri) are initialised at the superior-most centroids. At each iteration, the vertical discrepancy $|l_{li}y - r_{ri}y|$ is compared against a tolerance *thres*, which reflects the expected inter-level spacing of vertebrae. If the discrepancy is within tolerance, (l_{li}, r_{ri}) is recorded as a valid spinal pair, and both indices advance to the next level. Otherwise, the index corresponding to the centroid located higher (larger y in image space) is incremented, allowing the algorithm to realign when one side contains missing or spurious detections (Figure 5).

This robust two-pointer strategy ensures one-to-one, order-preserving vertebral matches with linear complexity $O(n + m)$ and minimal memory overhead, ideal for large-scale datasets. As shown in Figure 5, DPL establishes bilateral correspondences from superior to inferior vertebrae, gracefully handling skipped levels and noisy detections. Enforcing anatomical consistency and vertical alignment, it yields stable spinal landmark pairings that provide a reliable foundation for automatic UCA.

ALGORITHM 2 | Dynamic Pairing Logic algorithm

Require: Lists of left centroids $L = l_1, l_2, ..., l_n$, right centroids $R = r_1, r_2, ..., r_m$, angle threshold *thres*
Ensure: List of index pairs (i, j) where l_i matches r_j

```
li ← 0
ri ← 0
n ← length(L)
m ← length(R)
pairs ← empty list
while li < n and ri < m do
    if |L_li^y − R_ri^y| < thres then
        append (li, ri) to pairs
        li ← li + 1
        ri ← ri + 1
    else if L_li^y > R_ri^y then
        li ← li + 1
    else
        ri ← ri + 1
    end if
end while
return pairs
```

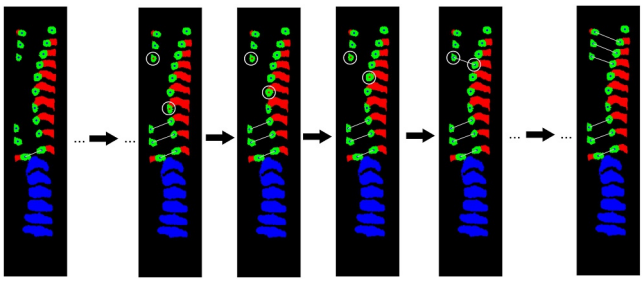


FIGURE 5 | Visualisation of the Dynamic Pairing Logic (DPL) algorithm. Vertically ordered centroids from left and right spinal features are sequentially compared under a tolerance constraint. Mismatched detections (circled) trigger adaptive index advancement, enabling robust realignment and one-to-one vertebral pairing.

Because direct ground-truth annotations for intermediate vertebral pairings are unavailable, the tolerance threshold *thres* (set to 150 pixels in our implementation) was determined through downstream task optimisation. Specifically, *thres* was optimised via empirical testing to minimise the Average Absolute Difference (ABS) between the final predicted Ultrasound Curve Angle (UCA). Subsequent sensitivity analysis confirmed that the pairing algorithm remains stable and robust to minor variations around this optimal threshold.

Specifically, there are two steps. In the first step, each detected spinal line is assigned a polarity sign ("+" or "–") according to its orientation with respect to the horizontal axis. Consecutive lines with consistent polarity are then grouped into anatomical segments, representing contiguous regions of similar curvature. To ensure robustness, only runs of at least three identical signs are considered as valid segments, while shorter runs are merged with the preceding group (The procedure is illustrated in Algorithm 3 and Figure 6).

In the second step, angular deviations are computed between consecutive segment pairs. For each pair, the maximum local angle between adjacent segments is calculated using the formula:

$$\theta = \arctan\left(\frac{|m_1 - m_2|}{1 + m_1 m_2}\right) \cdot \frac{180}{\pi}, \tag{3}$$

where m_1 and m_2 denote the slopes of two lines within adjacent segments. This ensures that the sharpest local deflection is

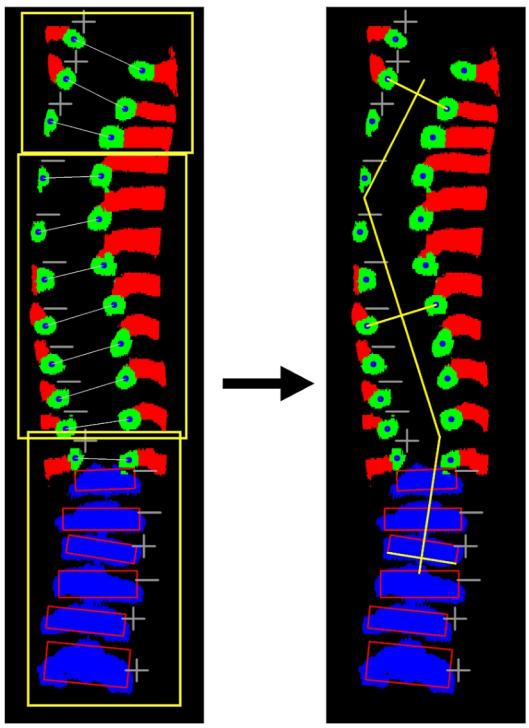


FIGURE 6 | Angle detection procedure on spinal ultrasound images. (Left) segmented spinal landmarks are annotated with polarity signs ("+" or "–") based on line orientation relative to the horizontal axis. Consecutive runs of identical signs are grouped into anatomical segments (yellow boxes). (right) For each adjacent segment pair, the maximum inter-line angle is computed (yellow connecting lines), providing quantitative curvature measures along the spinal axis.

captured, thereby representing the curvature transition between spinal regions. If only one segment is present, the maximum internal angle among all its lines is used.

Figure 6 demonstrates the outcome of the method. On the left, polarity signs are annotated to each spinal line, and yellow boxes highlight contiguous segments. On the right, yellow connecting lines indicate angular measurements extracted from segment boundaries, providing a quantitative representation of spinal curvature.

ALGORITHM 3 | Angle Detection Algorithm

Require: Spinal lines $P = p_1, p_2, ..., p_n$

Ensure: List of UCA

Step 1: Annotate signs to spinal lines;

Initialise empty *signs*
for $i = 1$ to n **do**
  $l \leftarrow P_i[Left]$
  $r \leftarrow P_i[Right]$
  $\theta \leftarrow |\text{atan2}(r^y - l^y,\ r^x - l^x)| \cdot \frac{180}{\pi}$
  if $\theta \geq 0$ **then**
    $signs \leftarrow +$
  else
    $signs \leftarrow -$
  end if
end for

Step 2: Segment grouping;

Initialize empty *segments*;
for $i = 1$ to $length(signs)$ **do**
  Consecutive runs of at least 3 identical signs form a new *segment*;
  $segments \leftarrow segment$
end for

Step 3: Angle computation;

Initialize empty *angles*;
for each consecutive segment pair (S_k, S_{k+1}) **do**
  Compute maxCalculateAngle$(p, q) : p \in S_k, q \in S_{k+1}$ and append to *angles*;
end for

return *angles*;

This automated angle detection framework eliminates manual annotation, reduces inter-observer variability, and provides reproducible measurements of spinal curves in ultrasound imaging. By combining polarity-based grouping with maximum angle computation, the method is both computationally efficient and robust to local detection errors, offering a reliable basis for scoliosis assessment and other spinal deformity analyses.

4 | Experiment Setting

4.1 | Dataset

This research utilises 3D ultrasound imaging data acquired from the Scolioscan system (as Figure 7 shows), which generates volumetric projection images (VPI) of the spine. The dataset consists of two versions.



FIGURE 7 | ScolioScan Machine. The ScolioScan system is used for ultrasound-based scoliosis assessment.

Version 1 includes 109 patients (82 females and 27 males) with an average age of 15.6 ± 2.7 years, an average Cobb angle of 25.5 ± 9.6°, and a body mass index (BMI) of 16.8 ± 3.6. All data were manually annotated with corresponding segmentation masks by clinical experts at The Hong Kong Polytechnic University [1].

Version 2 contains 200 paired samples, each consisting of an ultrasound image and its corresponding annotation.

Furthermore, all the bone features are illustrated in Figure 8. The Lumbar Bone Features, marked in blue, and the Thoracic Bony Features, highlighted in red and green, are the key anatomical features labelled by expert annotators. Ethical approval for this study was granted by the Hong Kong Polytechnic University Ethics Committee (approval number: HSEARS20180906005).

4.2 | Implementation

All experiments were conducted on a remote server provided by the University of Technology Sydney, equipped with two NVIDIA A40 GPUs (48 GB each), using Python 3.10 and PyTorch 2.4.0. The dataset consists of grayscale ultrasound images and corresponding labels stored in NumPy `.npz` format. Image intensities were normalised to the range [0, 255], and label values were restricted to discrete classes (0, 1, 2, and 3). The data were randomly split into training, validation, and testing sets in an 80:10:10 ratio. Input images were resized to

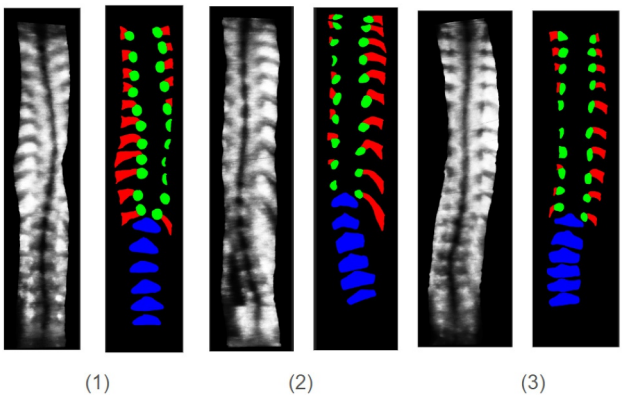


FIGURE 8 | Bone feature. The left image in each pair shows the original ultrasound image, while the right image displays the manual label.

224 × 224 pixels (window size = 7, patch size = 4) and standardised before training. The model was trained for 200 epochs using the Adam optimiser with an initial learning rate of 1×10^{-3} and a batch size of 12. A cosine annealing learning rate schedule was applied to improve convergence stability. To enhance robustness, data augmentation techniques were employed, including random rotations, horizontal flipping, Gaussian noise injection, contrast adjustment, and elastic deformation. During evaluation, predictions were restored to the original resolution of 640 × 2580 pixels. Performance was reported using both the original class labels and a merged class setting (where classes 1 and 2 were combined).

4.3 | Evaluation Metrics

We first evaluate the segmentation performance of *ISC-Swin* using two commonly adopted metrics: *Dice Similarity Coefficient* (*DSC*) and *Intersection over Union* (*IoU*). These metrics provide a standard assessment of the overlap between the predicted segmentation and the ground truth.

In addition, UCA measurements are derived from the segmentation outputs [3], and the *ABS* (Average Absolute Difference) is introduced to quantify prediction accuracy across numerical ranges:

$$\text{ABS} = \text{Absolute Value}(|\text{Ground Truth} - \text{Prediction}|). \quad (4)$$

Furthermore, to evaluate the model's capability in the final downstream task, we conduct statistical analyses.

5 | Result

5.1 | Segmentation Comparison Result

For the evaluation of version 1, we compared our proposed ISC-Swin model with several Transformer-based networks (Swin-Unet, H2Former, TransUnet, TransDeepLab, SegFormer, and SATR) and conventional U-Net variants (U-net and U-net++) for bone feature detection. The results are presented in Table 1.

The ISC-Swin model outperformed all other models, achieving the highest DSC (86.10%) and IoU (76.08%). Among the Transformer-based networks, SATR and SegFormer performed similarly with DSC values of 85.81% and 83.67%, and IoU values of 75.81% and 72.66%, respectively. H2Former and Swin-Unet followed closely with DSC values of 84.70% and 84.50%, while TransUnet and TransDeepLab showed slightly lower performance. Conventional U-Net variants, U-net and U-net++, achieved DSC scores of 81.9% and 82.20%, with IoU values of 69.20% and 69.40%, respectively.

We also compared the dice score for two classes (LBFs, TBFs) for ISC-Swin, Swin-Unet, and TransUnet, averaged over 8 validation trials. The result is shown as Table 2. In detail, ISC-Swin achieves the highest average performance for Class 1 (83.2%) with a standard deviation of 0.8, which is lower than both Swin 1.2 and TransUnet 1.7, demonstrating more stable performance. For Class 2, ISC-Swin achieves the highest average score (84.3%) compared to both Swin (83.2%) and TransUnet (83.3%), while maintaining competitive stability with a standard deviation of 2.8. The baseline Swin model shows slightly lower performance in both classes.

In addition, we visualised all prediction results for a randomly selected case, displayed in white for clearer presentation and comparison purposes.

The ISC-Swin model provides the most accurate predictions, effectively capturing the complete spinal structure and fine-grained anatomical details (Figure 9). In particular, it demonstrates superior continuity and integrity in both thoracic and lumbar regions, even under challenging conditions such as limited field-of-view and low contrast. Swin-Unet and H2Former also achieve competitive performance, but exhibit minor blurring and occasional discontinuities in boundary regions. In contrast, TransUnet, TransUnet+, and TransDeepLab show degraded segmentation quality, with more pronounced structural fragmentation, noise, and missing features. Notably, ISC-Swin achieves more precise classification and separation of the upper TBF-1 and TBF-2 regions as well as the six LBF regions, producing predictions that closely align with the ground truth. This improvement can be attributed to the inter-sample contrastive enhancement and the transformer-based architecture, which together enhance feature consistency and capture long-range dependencies across the spine.

5.2 | Ablation Study

Table 3 provides a comprehensive comparison of model performance under different queue lengths (16, 32, and 64) and batch sizes (6, 12, and 16). The results demonstrate that extending the queue length generally enhances performance. In particular, a queue length of 64 achieves the highest scores on most metrics, including LBF-1 (79.1%), LBF-2 (76.8%), DSC (85.4%), and IoU (74.5%), whereas queue lengths of 16 and 32 yield comparable but slightly lower values. This indicates that a longer queue length contributes to more robust feature representation and improved training stability. Similarly, enlarging the batch size leads to noticeable improvements across most evaluation metrics. Although the highest LBF-1 score is observed at a batch size of 12 (79.1%), the configuration with 16 provides superior overall performance, particularly for TBF (84.7%), DSC (85.8%), and IoU (75.2%). This suggests that larger batch sizes facilitate more stable gradient estimation and better generalisation.

TABLE 2 | DSC comparison for two classes on the validation set (%).

	LBF			TBF		
Case	**ISC-Swin**	**Swin**	**TransUnet**	**ISC-Swin**	**Swin**	**TransUnet**
1	82.4	81.4	81.4	83.9	84.3	77.1
2	84.1	82.8	84.1	87.2	85.6	86.7
3	82.2	80.0	79.8	86.8	87.2	86.8
4	83.8	83.6	84.9	84.2	83.5	85.0
5	82.8	81.4	81.0	80.5	76.4	82.5
6	83.5	81.3	81.9	83.8	81.3	82.3
7	82.6	80.4	82.5	84.1	82.0	83.1
8	84.2	82.1	83.1	85.9	85.0	82.6
Avg	**83.2**	81.6	82.3	**84.3**	83.2	83.3
Std	**0.8**	1.2	1.7	**2.8**	3.3	3.1

Note: The best result for each metric is highlighted.

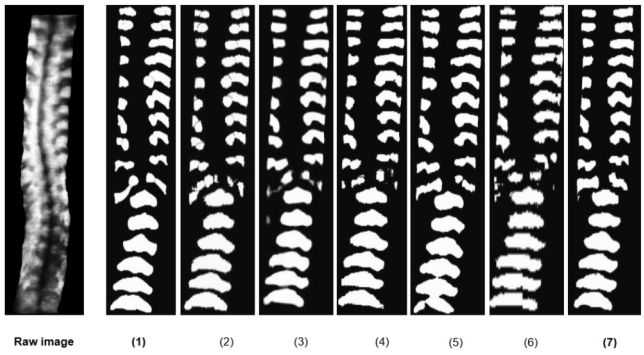


FIGURE 9 | Segmentation result. Raw sample with different performance for different models: (1) *Ground truth*, (2) H2Former, (3) Swin-Unet, (4) TransUnet, (5) TransUnet+, (6) TransDeepLab, (7) *ISC-Swin*.

TABLE 3 | Effect of queue length and batch size on performance (%).

Setting	**Value**	**LBF-1**	**LBF-2**	**TBF**	**DSC**	**IoU**
Queue length	16	78.8	76.4	83.2	85.1	74.2
	32	78.8	76.2	**83.3**	85.2	74.3
	64	**79.1**	**76.8**	83.2	**85.4**	**74.5**
Batch size	6	78.8	75.2	83.2	85.2	74.3
	12	**79.1**	75.8	84.1	85.7	75.0
	16	78.9	**76.3**	**84.7**	**85.8**	**75.2**

Note: LBF-1, LBF-2, and TBF denote DSC values for different bone features. The best result for each metric is highlighted.

5.3 | Statistical Analysis

Table 4 summarises the performance of three approaches—CPI-SLO, Auto-ISC, and Manual—in estimating the minimum and maximum UCA for both thoracic and lumbar regions. All values are reported in degrees (°). To provide a fair comparison with existing CPI-SLO–based methods, we followed the same evaluation protocol and excluded extreme outlier cases (defined as those with ABS greater than 5°).

Manual measurements are used as the reference standard and therefore do not include ABS values. Compared with the CPI-SLO variants, the proposed Auto-ISC method achieves UCA estimates that more closely approximate the manual annotations and yields reduced ABS in both the thoracic (2.83° ± 2.16°) and lumbar (2.89° ± 2.55°) regions. Consistent with prior studies, outlier cases were excluded for all methods to ensure a fair and standardised comparison.

In addition, the method achieves strong agreement with the manual result, with $R^2 = 0.91$ for thoracic and $R^2 = 0.81$ for lumbar regions (Figure 10).

The Bland–Altman analysis (Figure 11) demonstrated strong agreement between the proposed predictions and manual measurements. The mean difference (bias) was 0.62°(Thoracic) and 0.64° (Lumbar), with 95% limits of agreement ranging from [−7.77°, 9.01°] in Thoracic and [−6.80°, 8.07°] in Lumbar, indicating that most predictions fall within a clinically acceptable range. Moreover, nearly all data points were distributed within these limits, suggesting good consistency and no significant systematic deviation between the proposed method and manual measurements.

6 | Discussion

6.1 | Segmentation-Driven Angle Estimation

Enhanced segmentation performance facilitates more precise and complete centroid extraction, thereby mitigating positional noise and minimising missing detections. Consequently, this stabilises the Dynamic Pairing Logic (DPL) framework by ensuring consistent spatial ordering and reducing ambiguity in tolerance-based matching. As a result, the overall UCA estimation achieves greater robustness and clinical reliability, as evidenced by the reduced variability—specifically, a significantly lower standard deviation (approximately 1.5°) in ABS(T)—and a 0.5° reduction in mean ABS(L) (Table 4).

6.2 | Missing Feature

Ultrasound imaging is highly operator-dependent due to its narrow field of view and inherent artefacts such as acoustic shadowing and speckle noise [3, 15]. Although our model demonstrates strong correlation with manual annotations,

TABLE 4 | Comparison of UCA estimation ranges and errors among automated and manual methods (°).

Method	Range (*T*)	Range (*L*)	ABS (*T*)	ABS (*L*)
U-Net (CPI-SLO)	5.01–53.31	5.24–50.52	—	—
SEAM (CPI-SLO)	4.17–62.77	5.24–48.31	—	—
JSSNR (CPI-SLO)	6.86–53.44	7.20–49.91	**2.82** ± 3.62	3.34 ± 2.93
Auto-ISC	6.02–53.48	6.40–48.60	2.83 ± **2.16**	**2.89** ± **2.55**
Manual	7.90–59.90	10.40–47.20	—	—

Note: Range (T/L): range of thoracic/lumbar curvature angles; ABS (T/L): absolute UCA error (mean ± standard deviation). The best result for each metric is highlighted.

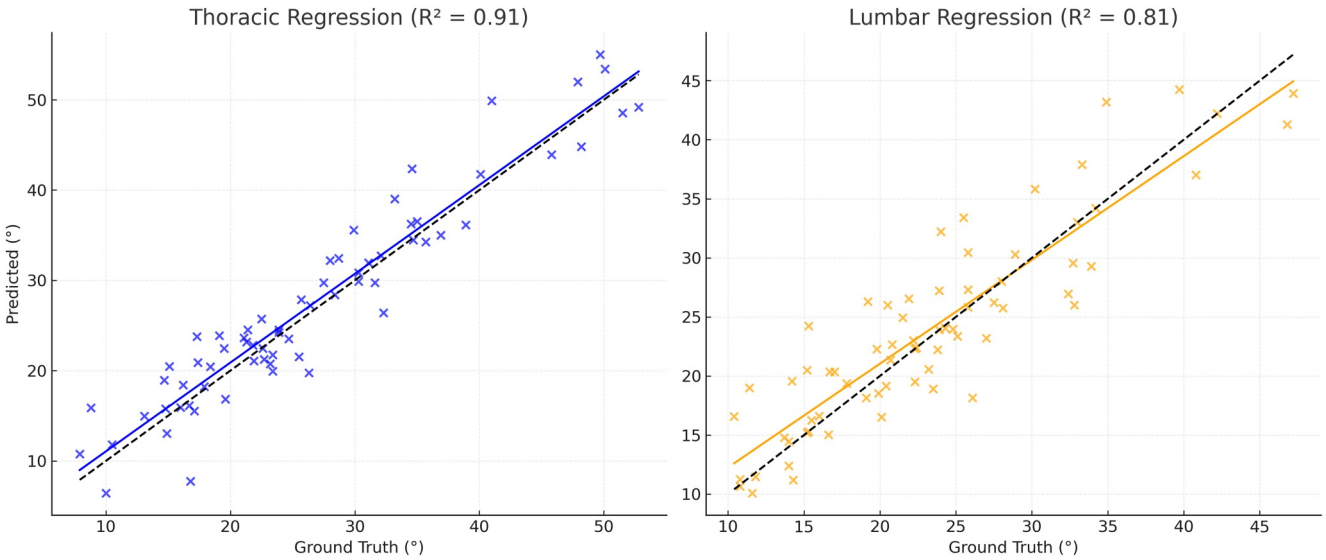


FIGURE 10 | Regression analysis of the proposed Auto-ISC for thoracic (left) and lumbar (right) UCA estimation. Each scatter plot shows the relationship between predicted angles and manual ground-truth measurements. Solid lines represent the regression fit, and dashed lines denote the identity line ($y = x$).

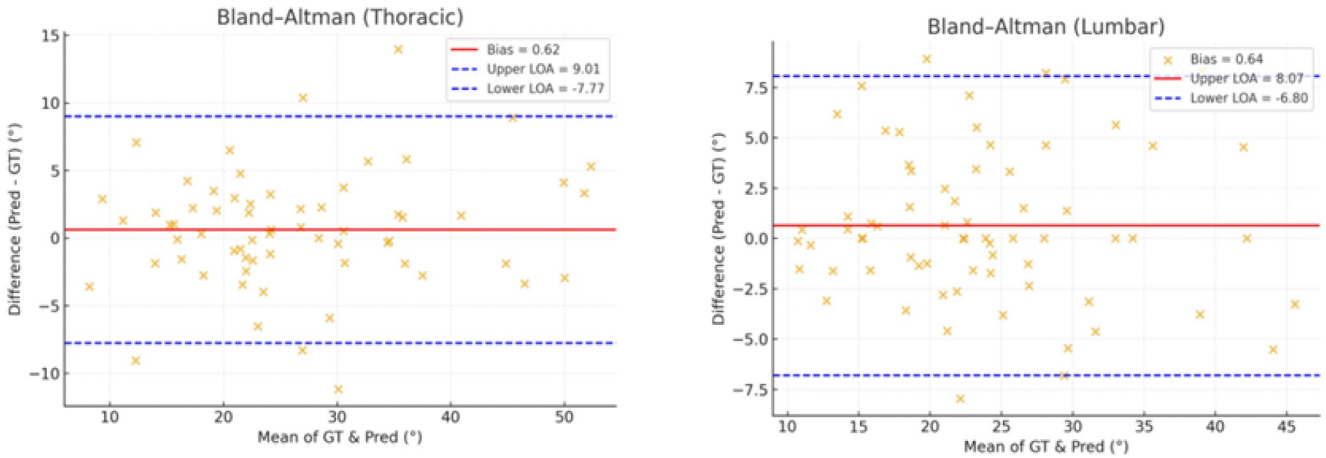


FIGURE 11 | Bland–Altman plots illustrating the agreement between automated and manual UCA measurements for the thoracic (left) and lumbar (right) regions.

missing anatomical features—often caused by suboptimal probe placement or image quality—compromise its ability to accurately detect key structures, which is likely caused by higher prediction errors, as reflected in Table 4. These omissions also impair the dynamic pairing algorithm, which relies on consistent landmark visibility for reliable matching [46]. This highlights the sensitivity of automated systems to operator-induced variability in real-world ultrasound acquisition. It is worth noting that such missing-feature cases are primarily associated with challenging acquisition conditions (e.g., limited field-of-view or acoustic shadowing) and are relatively uncommon in routine clinical practice.

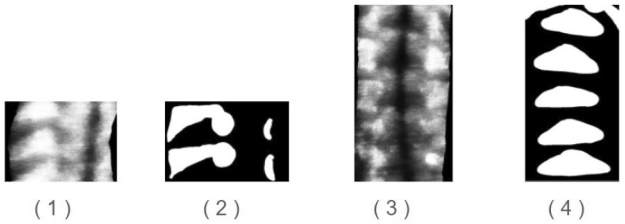


FIGURE 12 | Feature highlights for both thoracic and lumbar regions. (a, b) Thoracic features and the corresponding mask; (c, d) lumbar features and the corresponding mask.

6.3 | Failure Lumbar Landmark

The lumbar region in the ultrasound scenario, as shown in Figure 12, lacks clear anatomical boundaries—adjacent vertebral structures are often conjoined. Consequently, accurate separation of individual lumbar vertebrae relies heavily on extensive clinical expertise, posing significant challenges for both segmentation and landmark detection.

Compared with CNN-based methods, Auto-ISC reduces fragmented predictions and missing anatomical structures, particularly in thoracic regions affected by limited field-of-view. This is mainly attributed to the inter-sample contrastive enhancement, which improves feature consistency across samples, and the transformer-based architecture that captures long-range dependencies. However, residual errors still occur in regions with severe acoustic shadowing and low signal-to-noise ratio, indicating the inherent limitation of ultrasound imaging.

6.4 | Superiority of Dynamic Pairing Logic

Figure 6 demonstrates the outcome of the method. On the left, polarity signs are annotated to each spinal line, and yellow boxes highlight contiguous segments. On the right, yellow connecting lines indicate angular measurements extracted from segment boundaries, providing a quantitative representation of spinal curvature. This automated angle detection framework eliminates manual annotation, reduces inter-observer variability, and provides reproducible measurements of spinal curves in ultrasound imaging. By combining polarity-based grouping with maximum angle computation, the method is both computationally efficient and robust to local detection errors, offering a reliable basis for scoliosis assessment and other spinal deformity analyses.

Importantly, the proposed dynamic pairing logic is specifically designed to address the incomplete feature problem caused by the limited field-of-view (FOV) in ultrasound imaging. In practice, thoracic landmarks are frequently partially visible or entirely missing due to acoustic shadowing, occlusion, and scanning constraints, leading to fragmented or discontinuous segmentation outputs. Conventional methods that rely on strict one-to-one correspondence between detected landmarks are highly sensitive to such missing features, often resulting in incorrect or unstable angle estimation. In contrast, our method introduces a polarity-based grouping and flexible pairing strategy, which allows structurally consistent segments to be adaptively matched even when intermediate features are absent. By focussing on global structural continuity rather than local completeness, the algorithm effectively mitigates errors caused by missing thoracic points and reduces the impact of segmentation discontinuities.

From a clinical perspective, the proposed Auto-ISC system simplifies the scoliosis assessment workflow by eliminating manual landmark identification and enabling fully automated UCA estimation from ultrasound images. Compared with traditional Scolioscan-based analysis, which still relies on operator-dependent interpretation, our method provides more consistent and reproducible measurements. In addition, the radiation-free nature of ultrasound, combined with automated processing, makes the proposed system suitable for large-scale scoliosis screening and longitudinal monitoring in clinical practice.

6.5 | Impact of the Inter-Sample Contrastive Bank on Pixel-Level Feature Enhancement

The Inter-Sample Contrastive Bank (ISCB) significantly improves ultrasound scoliosis segmentation by enhancing feature representation through enriched attention mechanisms, hierarchical feature learning, and adaptive sampling. This leads to more accurate pixel-level discrimination and overall performance gains. Quantitatively, the inclusion of ISCB results in an increase in DSC of approximately 1%–5% overall. Additional improvements are observed with larger batch sizes, yielding further gains of approximately 0.1% in DSC, along with increases of about 0.4% and 0.6% in DSC and IoU, respectively.

Furthermore, pixel-level contrast enhancement plays a critical role in improving segmentation performance. As illustrated in Figure 12, the trailing region of the TBF (denoted as TBF-2) exhibits significantly lower contrast with the background compared to the leading region (TBF-1), making it more challenging to segment. This ambiguity can be effectively mitigated by introducing an additional task head, which enhances feature discrimination in low-contrast regions and further improves overall segmentation performance.

7 | Conclusion

This paper presents Auto-ISC, a novel two-stage automated ultrasound scoliosis assessment system that addresses key limitations in radiation-free scoliosis diagnosis. The proposed framework integrates the ISC-Swin segmentation model with an Inter-Sample Contrastive Bank to enhance bone feature representation, along with a Dynamic Pairing Logic algorithm for accurate thoracic vertebrae matching. Experimental results demonstrate improved segmentation performance and clinically reliable Ultrasound Curve Angle (UCA) estimation, achieving low average absolute difference (ABS) compared with manual UCA measurements.

Future work should focus on enhancing the robustness and generalisability of feature extraction across all anatomical regions, especially the lumbar spine, where boundaries are often unclear. This includes developing advanced deep learning methods capable of handling missing or ambiguous features, incorporating multi-view or 3D contextual information, and leveraging self-supervised or contrastive learning for improved

feature consistency. Comprehensive experiments should evaluate performance across diverse environmental conditions, such as variations in imaging devices, operator expertise, patient anatomy, and image quality. This is particularly evident under extreme acquisition conditions, such as manual scanning errors. Integrating operator-in-the-loop guidance and uncertainty estimation could further improve clinical reliability or example, generative AI (GenAI) models could be leveraged to predict and restore missing anatomical features, thereby enhancing robustness in challenging cases. Future work will also include validation on larger multi-centre datasets and prospective clinical studies to further assess generalisability and real-world applicability. These efforts would advance Auto-ISC towards a fully robust, radiation-free scoliosis assessment tool suitable for routine screening and longitudinal monitoring while minimising patient radiation exposure.

Acknowledgement

Open access publishing facilitated by University of Technology Sydney, as part of the Wiley - University of Technology Sydney agreement via the Council of Australasian University Librarians.

Funding

The authors have nothing to report.

Conflicts of Interest

Sai Ho Ling is an Editorial Board Members for the journal, and was not involved in peer review process or the decision to publish this article. The authors declare that they have no conflict of interest.

Data Availability Statement

The data that support the findings of this study are available on request from the corresponding author. The data are not publicly available due to privacy or ethical restrictions.

References

1. C.-W. J. Cheung, G.-Q. Zhou, S.-Y. Law, T.-M. Mak, Ka-L. Lai, and Y.-P. Zheng, "Ultrasound Volume Projection Imaging for Assessment of Scoliosis," *IEEE Transactions on Medical Imaging* 34, no. 8 (2015): 1760–1768, https://doi.org/10.1109/tmi.2015.2390233.

2. H. Kim, H. S. Kim, E. S. Moon, et al., "Scoliosis Imaging: What Radiologists Should Know," *Radiographics* 30, no. 7 (2010): 1823–1842, https://doi.org/10.1148/rg.307105061.

3. Y.-P. Zheng, T. T.-Y. Lee, K. Ka-L. Lai, et al., "A Reliability and Validity Study for Scolioscan: A Radiation-Free Scoliosis Assessment System Using 3d Ultrasound Imaging," *Scoliosis and Spinal Disorders* 11 (2016): 1–15, https://doi.org/10.1186/s13013-016-0074-y.

4. J. Cobb, "Outline for the Study of Scoliosis," *Instructional Course Lecture* (1948).

5. A. R. Levy, M. S. Goldberg, N. E. Mayo, J. A. Hanley, and B. Poitras, "Reducing the Lifetime Risk of Cancer From Spinal Radiographs Among People With Adolescent Idiopathic Scoliosis," *Spine* 21, no. 13 (1996): 1540–1547, https://doi.org/10.1097/00007632-199607010-00011.

6. C. Huang, H. Tang, W. Fan, et al., "Fully-Automated Analysis of Scoliosis From Spinal x-Ray Images," in *2020 IEEE 33rd International Symposium on Computer-Based Medical Systems (CBMS)* (IEEE, 2020), 114–119.

7. M. Zhao, N. Meng, J. P. Yin Cheung, C. Yu, P. Lu, and T. Z. Spinehrformer, "A Transformer-Based Deep Learning Model for Automatic Spine Deformity Assessment With Prospective Validation," *Bioengineering* 10, no. 11 (2023): 1333, https://doi.org/10.3390/bioengineering10111333.

8. Y. Cui, J. Zhu, Z. Duan, Z. Liao, S. Wang, and W. Liu, "Artificial Intelligence in Spinal Imaging: Current Status and Future Directions," *International Journal of Environmental Research and Public Health* 19, no. 18 (2022): 11708, https://doi.org/10.3390/ijerph191811708.

9. R. C. Brink, S. P. J. Wijdicks, I. N. Tromp, et al., "A Reliability and Validity Study for Different Coronal Angles Using Ultrasound Imaging in Adolescent Idiopathic Scoliosis," *Spine Journal* 18, no. 6 (2018): 979–985, https://doi.org/10.1016/j.spinee.2017.10.012.

10. J. Alison Noble and D. Boukerroui, "Ultrasound Image Segmentation: A Survey," *IEEE Transactions on Medical Imaging* 25, no. 8 (2006): 987–1010, https://doi.org/10.1109/tmi.2006.877092.

11. Y. Yao, W. Yu, Y. Gao, et al., "W-Transformer: Accurate Cobb Angles Estimation by Using a Transformer-based Hybrid Structure," *Medical Physics* 49, no. 5 (2022): 3246–3262, https://doi.org/10.1002/mp.15561.

12. Y. Tang, H. Chen, L. Qian, S. Ge, M. Zhang, and R. Zheng, "Detection of Spine Curve and Vertebral Level on Ultrasound Images Using detr," in *2022 IEEE International Ultrasonics Symposium (IUS)* (IEEE, 2022), 1–4.

13. J. Lyu, S. Ho Ling, S. Banerjee, et al., "Ultrasound Volume Projection Image Quality Selection by Ranking From Convolutional Ranknet," *Computerized Medical Imaging and Graphics* 89 (2021): 101847, https://doi.org/10.1016/j.compmedimag.2020.101847.

14. C. Zhang, X. Deng, and S. Ho Ling, "Next-Gen Medical Imaging: U-Net Evolution and the Rise of Transformers," *Sensors* 24, no. 14 (2024): 4668, https://doi.org/10.3390/s24144668.

15. C. Zhang, Y. Zheng, J. McAviney, and S. Ho Ling, "Ssat-Swin: Deep Learning-Based Spinal Ultrasound Feature Segmentation for Scoliosis Using Self-Supervised Swin Transformer," *Ultrasound in Medicine & Biology* (2025).

16. S. Banerjee, J. Lyu, Z. Huang, et al., "Light-Convolution Dense Selection u-Net (Lds u-Net) for Ultrasound Lateral Bony Feature Segmentation," *Applied Sciences* 11, no. 21 (2021): 10180, https://doi.org/10.3390/app112110180.

17. Y. Zhou, Z. Huang, T. T.-Y. Lee, et al., "Morphological-Consistent Diffusion Network for Ultrasound Coronal Image Enhancement," *arXiv preprint arXiv:2409.16661* (2024).

18. H.-D. Wu, W. Liu, and M.-S. Wong, "Reliability and Validity of Lateral Curvature Assessments Using Clinical Ultrasound for the Patients With Scoliosis: A Systematic Review," *European Spine Journal* 29, no. 4 (2020): 717–725, https://doi.org/10.1007/s00586-019-06280-y.

19. S. L. Weinstein, L. A. Dolan, J. C. Y. Cheng, A. Danielsson, and J. A. Morcuende, "Adolescent Idiopathic Scoliosis," *lancet* 371, no. 9623 (2008): 1527–1537, https://doi.org/10.1016/s0140-6736(08)60658-3.

20. C. Zhang, W. Jia, Y. Zheng, and S. Ho Ling, "Isc-Swin: Inter Sample Contrastive Enhancement for Swin-Transformer in Ultrasound Spine Feature Segmentation," in *2025 IEEE International Conference on Systems, Man, and Cybernetics (SMC)* (IEEE, 2025), 1505–1510.

21. H. Xie, Z. Huang, F. H. F. Leung, et al., "A Structure-Affinity Attention-Based Transformer Encoder for Spine Segmentation," in *2024 IEEE International Symposium on Biomedical Imaging (ISBI)* (IEEE, 2024), 1–5.

22. E. Xie, W. Wang, Z. Yu, A. Anandkumar, J. M. Alvarez, and P. Luo, "SegFormer: Simple and Efficient Design for Semantic Segmentation With Transformers." in *Advances in Neural Information Processing Systems* vol. 34 (2021), 12077–12090, https://doi.org/10.5555/3540261.3541185.

23. Hu Cao, Y. Wang, J. Chen, et al., "Swin-Unet: Unet-Like Pure Transformer for Medical Image Segmentation," in *European Conference on Computer Vision* (Springer, 2022), 205–218.

24. A. He, K. Wang, T. Li, C. Du, S. Xia, and H. Fu, "H2former: An Efficient Hierarchical Hybrid Transformer for Medical Image Segmentation," *IEEE Transactions on Medical Imaging* (2023).

25. J. Chen, Y. Lu, Q. Yu, et al., "Transunet: Transformers Make Strong Encoders for Medical Image Segmentation," *arXiv preprint arXiv: 2102.04306* (2021).

26. R. Azad, M. Heidari, M. Shariatnia, et al., "Transdeeplab: Convolution-Free Transformer-Based Deeplab v3+ for Medical Image Segmentation," in *International Workshop on PRedictive Intelligence In MEdicine* (Springer, 2022), 91–102.

27. O. Ronneberger, P. Fischer, and T. Brox, "U-Net: Convolutional Networks for Biomedical Image Segmentation," in *Medical Image Computing and Computer-Assisted Intervention–MICCAI 2015: 18Th International Conference, Munich, Germany, October 5-9, 2015, Proceedings, Part III 18* (Springer, 2015), 234–241.

28. Z. Zhou, Md M. R. Siddiquee, N. Tajbakhsh, and J. Liang, "Unet++: A Nested u-Net Architecture for Medical Image Segmentation," in *Deep Learning in Medical Image Analysis and Multimodal Learning for Clinical Decision Support: 4Th International Workshop, DLMIA 2018, and 8th International Workshop, ML-CDS 2018, Held in Conjunction with MICCAI 2018, Granada, Spain, September 20, 2018, Proceedings 4* (Springer, 2018), 3–11.

29. A. Rykkje, J. F. Carlsen, and M. B. Nielsen, "Hand-Held Ultrasound Devices Compared With High-end Ultrasound Systems: A Systematic Review," *Diagnostics* 9, no. 2 (2019): 61, https://doi.org/10.3390/diagnostics9020061.

30. S.-Y. Ng and J. Bettany-Saltikov, "Imaging in the Diagnosis and Monitoring of Children With Idiopathic Scoliosis," *Open Orthopaedics Journal* 11, no. 1 (2017): 1500–1520, https://doi.org/10.2174/1874325001711011500.

31. R. N. Uppot, "Technical Challenges of Imaging & Image-Guided Interventions in Obese Patients," *British Journal of Radiology* 91, no. 1089 (2018): 20170931, https://doi.org/10.1259/bjr.20170931.

32. M. J. Modica, K. M. Kanal, and M. L. Gunn, "The Obese Emergency Patient: Imaging Challenges and Solutions," *Radiographics* 31, no. 3 (2011): 811–823, https://doi.org/10.1148/rg.313105138.

33. A. Majeed, A. Abuhamad, L. Romary, and E. Sinkovskaya, "Can Ultrasound in Early Gestation Improve Visualization of Fetal Cardiac Structures in Obese Pregnant Women?," *Journal of Ultrasound in Medicine* 38, no. 8 (2019): 2057–2063, https://doi.org/10.1002/jum.14895.

34. R. Strony, "Ultrasound-Assisted Lumbar Puncture in Obese Patients," *Critical Care Clinics* 26, no. 4 (2010): 661–664, https://doi.org/10.1016/j.ccc.2010.07.002.

35. T. Ungi, F. King, M. Kempston, et al., "Spinal Curvature Measurement by Tracked Ultrasound Snapshots," *Ultrasound in Medicine & Biology* 40, no. 2 (2014): 447–454, https://doi.org/10.1016/j.ultrasmedbio.2013.09.021.

36. S. Banerjee, J. Lyu, Z. Huang, et al., "Ultrasound Spine Image Segmentation Using Multi-Scale Feature Fusion Skip-Inception U-Net (SIU-Net)," *Biocybernetics and Biomedical Engineering* 42, no. 1 (2022): 341–361, https://doi.org/10.1016/j.bbe.2022.02.011.

37. Yi Huang, J. Jiao, J. Yu, Y. Zheng, and Y. Wang, "Rsalunet: A Reinforcement Supervision U-Net-Based Framework for Multi-ROI Segmentation of Medical Images," *Biomedical Signal Processing and Control* 84 (2023): 104743, https://doi.org/10.1016/j.bspc.2023.104743.

38. L. Cohen Monteiro, Y. Zheng, and S. Ho Ling, "A Improved Hybrid Attention Recurrent Residual U-Net Approach for the Segmentation of Ultrasound Spine Images," *Biomedical Signal Processing and Control* 108 (2025): 107925, https://doi.org/10.1016/j.bspc.2025.107925.

39. H. Xie, Z. Huang, Y. Zuo, et al., "Sa^2Net: Scale-Adaptive Structure-Affinity Transformation for Spine Segmentation From Ultrasound Volume Projection Imaging," *Computerized Medical Imaging and Graphics* 125 (2025): 102649, https://doi.org/10.1016/j.compmedimag.2025.102649.

40. Z. Huang, R. Zhao, F. H. F. Leung, et al., "Joint Spine Segmentation and Noise Removal From Ultrasound Volume Projection Images With Selective Feature Sharing," *IEEE Transactions on Medical Imaging* 41, no. 7 (2022): 1610–1624, https://doi.org/10.1109/tmi.2022.3143953.

41. S. Dana, C. Zhang, Y. Zheng, and S. Ho Ling, "Vertebra-Level Completeness Analysis in Thoracolumbar Ultrasound Using a Yolo-Based Detection Framework," *Sensors* (2026).

42. S. Banerjee, Z. Huang, J. Lyu, et al., "Automatic Assessment of Ultrasound Curvature Angle for Scoliosis Detection Using 3-d Ultrasound Volume Projection Imaging," *Ultrasound in Medicine & Biology* 50, no. 5 (2024): 647–660, https://doi.org/10.1016/j.ultrasmedbio.2023.12.015.

43. Y. Zhou, T. T.-Y. Lee, K. Ka-L. Lai, et al., "Automatic Ultrasound Curve Angle Measurement via Affinity Clustering for Adolescent Idiopathic Scoliosis Evaluation," *Expert Systems with Applications* 269 (2025): 126410, https://doi.org/10.1016/j.eswa.2025.126410.

44. Yi Huang, J. Jiao, J. Yu, Y. Zheng, and Y. Wang, "Anatomy-Inspired Model for Critical Landmark Localization in 3d Spinal Ultrasound Volume Data," *Medical Image Analysis* 103 (2025): 103610, https://doi.org/10.1016/j.media.2025.103610.

45. M. Gutmann and A. Hyvärinen, "Noise-Contrastive Estimation: A New Estimation Principle for Unnormalized Statistical Models," in *Proceedings of the Thirteenth International Conference on Artificial Intelligence and Statistics* (JMLR Workshop and Conference Proceedings, 2010), 297–304.

46. I. Hacihaliloglu, "Ultrasound Imaging and Segmentation of Bone Surfaces: A Review," *Technology* 5, no. 2 (2017): 74–80, https://doi.org/10.1142/s2339547817300049.